Shock Waves
DOI 10.1007/s00193-016-0640-5

ORIGINAL ARTICLE

Characterizing pyrotechnic igniter output with high-speed schlieren imaging

M. N. Skaggs[1] · **M. J. Hargather**[2] · **M. A. Cooper**[3]

Received: 10 June 2015 / Revised: 12 February 2016 / Accepted: 23 February 2016

Abstract Small-scale pyrotechnic igniter output has been characterized using a high-speed schlieren imaging system for observing critical features of the post-combustion flow. The diagnostic, with laser illumination, was successfully applied towards the quantitative characterization of the output from Ti/$KClO_4$ and $TiH_{1.65}$/$KClO_4$ pyrotechnic igniters. The high-speed image sequences showed shock motion, burned gas expansion, and particle motion. A statistical-based analysis methodology for tracking the full-field shock motion enabled straightforward comparisons across the experimental parameters of pyrotechnic material and initial density. This characterization of the mechanical energy of the shock front within the post-combustion environment is a necessary addition to the large body of literature focused on pyrotechnic combustion behavior within the powder bed. Ultimately, understanding the role that the combustion behavior has on the resulting multiphase environment is required for tailored igniter development and comparative performance assessments.

Keywords Shock waves · Schlieren · High-speed imaging · Pyrotechnic

Communicated by L. Bauwens.

✉ M. N. Skaggs
mnskagg@sandia.gov

[1] Explosives Technologies Group, Sandia National Laboratories, PO Box 5800, Albuquerque, NM 87185-1452, USA

[2] Shock and Gas Dynamics Laboratory, New Mexico Institute of Technology, 120 Weir Hall, Socorro, NM 87801, USA

[3] Explosives Technologies Group, Sandia National Laboratories, PO Box 5800, Albuquerque, NM 87185-1454, USA

1 Introduction

A pyrotechnic hotwire igniter is an electro-explosive device (EED) that converts input electrical energy to mechanical pressure–volume work via an explosion [1]. The pyrotechnic material is thermally initiated through contact with a metal bridgewire that is heated with approximately 30 mJ of energy [2]. The thermally ignited pyrotechnic powder near the bridgewire transitions to a sustained combustion front that consumes the remaining material and releases exothermic energy into the surrounding environment [3]. Fundamental studies of the ignition and combustion characteristics of pyrotechnics [4–7], thermites [8,9], and intermetallics [10] have been conducted by numerous researchers where the material parameters of particle size, bed porosity, and mixture composition have been explored. In pyrotechnic EED development, the interplay between the igniter design aspects and the combustion behavior directly impact the energy released in the surrounding environment. Although many studies have characterized pyrotechnic materials, few studies have quantified overall igniter performance and shock wave output for actual igniter systems. The few published studies on EED device output primarily rely on computational simulations due to the experimental challenges in measuring and visualizing the multiphase, high-luminosity output flow [11,12]. This work overcomes the experimental challenges associated with qualitative and quantitative characterization of EED output and establishes the techniques useful for follow-on studies assessing the coupled effects of pyrotechnic burn behavior and EED design.

One challenge preventing predictions of EED device output is knowledge of the pyrotechnic combustion behavior within the device. It is well established that pyrotechnics may be characterized by a steady conductive burn where heat conduction dominates the energy transfer between unreacted

Published online: 15 March 2016

and reacted materials [13]. In this case, the surface regression rate r depends on the condensed phase density, burning surface area and pressure, and can be empirically correlated with Vieille's equation, $r = BP^n$, where B and n are fitted to closed bomb and/or strand burner data over specified ranges [14]. However, in pressed powder beds of pyrotechnics containing connected porosity, locally-varying density gradients, and no added binder, the gas pressures generated from the moving burn front may cause events such as powder grain or powder bed fragmentation, powder bed compaction, and flame acceleration into powder bed cracks or connective porosity.

The result of these phenomena is a deviation from a steady surface regression rate to convective or "progressive deconsolidation" [15] of the pyrotechnic. Characterization of both steady and unsteady burning modes within pyrotechnic mixtures by traditional closed bomb measurements [7,16–18] and with experiments intended to mimic EED confinement [19,20] have measured deflagration velocities spanning $10^{-1}-10^{3}$ m/s. As expected, the burning rate has a direct influence on the fraction of metal particle consumed within the device. When relatively short pyrotechnic beds (length-to-diameter ratio $\approx$1) are utilized in EED devices with weak axial confinement, post-ignition observations of solid particles entrained within a luminous jet of gaseous combustion products have been reported [21,22]. Studies on EED devices have yet to definitively correlate the presence of particles entrained in output flow to transition to the deconsolidated burning mode within the device. Clearly, the design aspects of the device confinement and powder bed characteristics will influence the resulting combustion behavior within the device and the observed multiphase output.

Prior experiments, each aimed at a particular EED application, have largely ignored the role that the combustion process within the device has on the quantified pressure–volume work [23], heat flux [24], and qualitatively visualized EED output with high-speed laser sheet photography [21,22]. Due to the pressures generated by these devices, characterization of the gas-dynamic shock behavior in the surrounding environment is a metric for inferring the pyrotechnic combustion behavior and performance differences impacted by device design. Traditional gas-dynamic diagnostic methods of schlieren, shadowgraphy, and holography have not been effectively applied to pyrotechnic EED outputs in any previous studies. High-speed schlieren imaging of shock waves from explosive micro-detonators fired into dynamic witness plates [25] and digital in-line holography of particle burning characteristics in propellant exhaust plumes [26] are the closest applications.

Kleine et al. [27,28] and Hargather et al. [29] have used schlieren and shadowgraph imaging techniques to characterize blast waves from high explosives at both milligram and gram scales, respectively, and to estimate their TNT equivalency through traditional blast wave scaling [30]. Blast properties of pyrotechnics have been measured previously and used to estimate TNT equivalency using pressure–time histories at locations from gram-scale charges [31,32]. Overpressure data were compared to TNT in terms of the scaled distance $R/W^{1/3}$, where R is the distance from the explosion and W is the pyrotechnic mass, quantifying a variable TNT equivalence. The usefulness of applying self-similar scaling relationships to analyze the output from the small-scale pyrotechnic EED devices is unknown given the expected violation of all point-blast assumptions [33].

In this new work, we have developed an experimental analysis methodology for characterizing the output from EED devices. This effort has focused on providing new images with high spatial and temporal resolution, clearly showing features of the multiphase output from pyrotechnic igniters. The features of interest include the shock wave expansion, combustion product gas plume growth, and the presence and subsequent motion of unburned solid particles. This imaging is achieved with state-of-the-art high power, effectively non-coherent laser illumination for imaging a large field of view surrounding our research EED device. The full-field shock behavior and expansion within the environment surrounding the device is quantitatively analyzed through statistical methods calculating a characteristic shock radius that varies with time, enabling straightforward comparisons across parameters of material and density. The shock wave behavior and qualitative features observed in the flow are used to infer differences in the combustion behavior within the device. This work establishes the experimental capability and analysis methodology, enabling follow-on studies exploring additional parameters of critical importance to the EED device design and performance community.

2 Pyrotechnic igniters

The research igniters used in this work have a header, a bridgewire, and a pyrotechnic charge pressed into a charge cavity that remained open to the surrounding environment (Fig. 1). Two titanium-based pyrotechnic materials used in industrial and research applications were studied: Ti/$KClO_4$ (TKP) and $TiH_{1.65}/KClO_4$ (THKP). In pyrotechnic igniters and actuators, performance is often characterized by the pressure–time history of the combustion gases used to drive pistons or perform mechanical work. Here, the igniter output of interest is the produced shock wave.

The TKP powder is a 33 % Ti and 67 % $KClO_4$ mixture by weight with nominal particle sizes of 13 and 14 μm, respectively. The THKP powder is a 33 % $TiH_{1.65}$ and 67 % $KClO_4$ mixture by weight with nominal particle sizes of 13 and 22 μm, respectively. Each igniter contained either TKP (15 mg ± 3 %) or THKP (16.6 mg ± 4.5 %) powder pressed

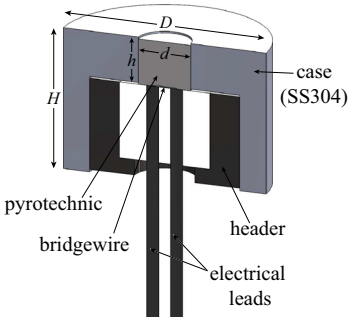

Fig. 1 Annotated illustration of research igniter showing header, bridgewire, and pyrotechnic pressed into the charge cavity. Dimensions of the cylindrical igniter body, $D = 0.856$ cm and $H = 0.589$ cm, and the charge cavity, $d = 0.221$ cm and $h = 0.191$ cm, are shown

Table 1 Test parameters of pyrotechnic igniters

Label	Material	ρ [g/cm^3]	$\phi \pm 0.02$	E [J]
T1	TKP	2.067 ± 0.070	0.70	16.9
T2	TKP	2.100 ± 0.066	0.71	17.9
T3	TKP	2.158 ± 0.059	0.73	20.2
TH2	THKP	2.278 ± 0.066	0.80	46.8
TH3	THKP	2.396 ± 0.050	0.84	55.5

to a bed height of 0.1851 ± 0.0072 cm within the charge cavity at three bulk densities. The pyrotechnic masses were limited based on the amount of powder that could be pressed into the charge cavity while remaining flush with or below the top surface of the igniter. The average densities, ρ, and solid volume fractions, ϕ, are given in Table 1. The solid volume fraction, ϕ, is found by dividing the pressed density, ρ, by the calculated theoretical maximum density, ρ_S, of 2.96 g/cm^3 for TKP and 2.85 g/cm^3 for THKP.

The total energy E for each mixture was calculated from the difference in enthalpies between the reactants and burned products at ambient temperature $T_0 = 300$ K. The thermochemical calculations for a constant volume explosion including only the interstitial air in the powder bed were performed with CHEETAH 7.0 [34]. The reported energy values (Table 1) assume that the Ti fuel completely reacts within the charge cavity. While this provides a consistent metric with which to compare mixtures on a per unit energy basis, it will be shown in later sections that it is unlikely that all of the chemical energy is released through complete combustion within the charge cavity.

3 Experimental design

The lens-based schlieren system used a Specialized Imaging SILUX640 laser light source and a Shimadzu HPV-2 high-speed camera (Fig. 2). The collimating and schlieren lenses were two plano-convex achromatic lenses (15.24 cm in diameter) imaging a nominal 8 cm × 8 cm field of view. Each igniter was positioned at the imaging object plane within an explosive test chamber [35]. The SILUX640 laser system, which produced light centered at 644 nm with 8-nm bandwidth, was used with a notch filter centered at 640 nm with 12-nm bandwidth to filter the intense broadband pyrotechnic chemiluminescence [35]. A 2.0 neutral density filter and an imaging lens system demagnified the image onto the camera CCD. The camera CCD was 2.07 cm wide × 1.72 cm tall with pixel sizes of 66.3 μm × 66.3 μm for a total image size of 312 × 260 pixels.

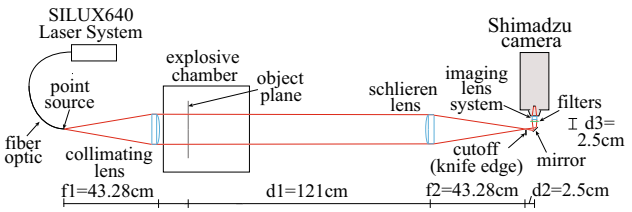

Fig. 2 Schematic of diagnostic setup using SILUX640 laser light source and Shimadzu HPV-2 high-speed camera

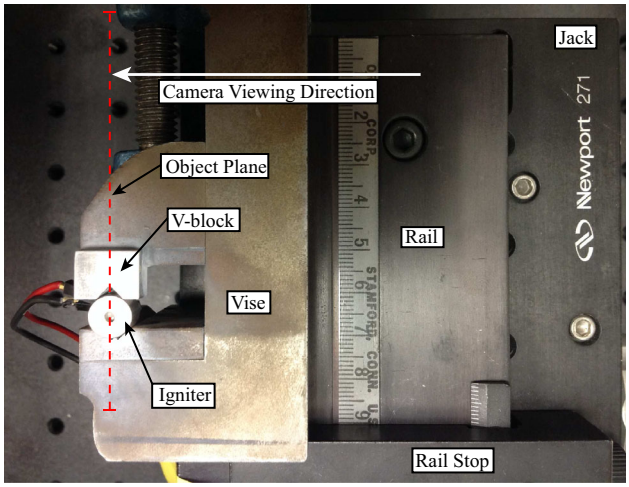

Fig. 3 Top-down view inside the explosive test chamber. The camera object plane is identified with a *red dashed line*

For each test, an igniter was secured in a vise with v-block jaws. Figure 3 shows a mounted igniter with annotations for the object plane and the camera viewing direction. The imaged field of view is shown to be offset toward the v-block jaws and that the top surfaces of the igniter body, v-block jaw and vise provide solid boundaries affecting the gas-dynamic flow.

The experiment timing depended on the trigger sequence required to couple the camera images, the laser pulses, and the current being monitored from the laser diode driver (LDD) [35]. Figure 4 presents the trigger diagram and associated timing diagram. The timing diagram shows the voltage signals as a function of time used to trigger the various events. The experiment was started by igniting the pyrotechnic with a

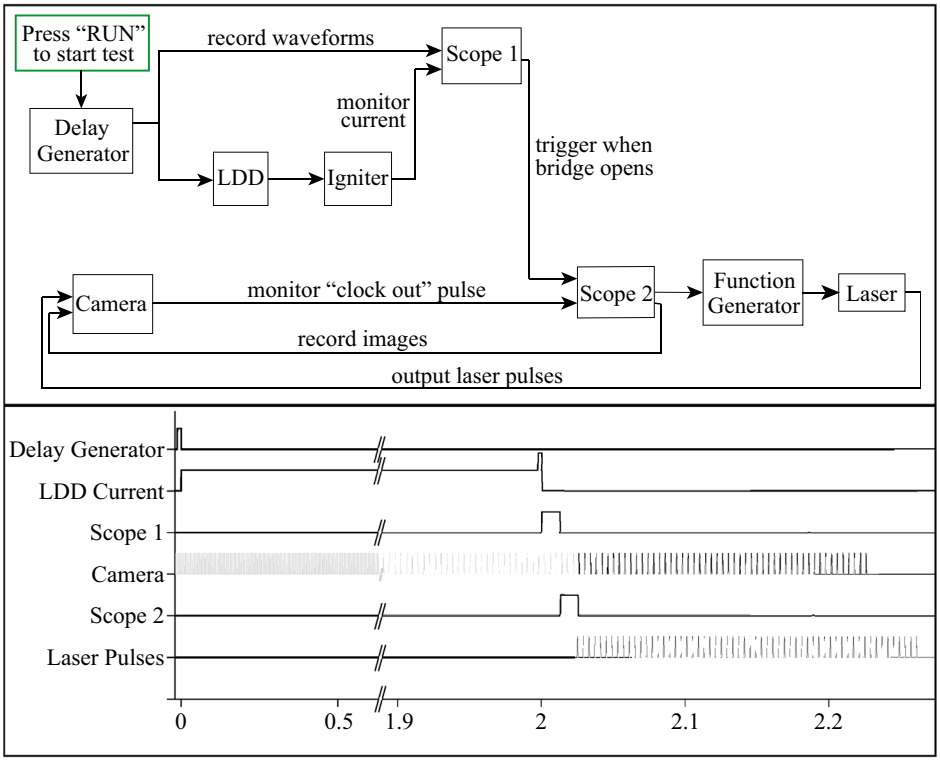

Fig. 4 (*Top*) Trigger diagram used with SILUX640 laser light source. (*Bottom*) Timing diagram used with SILUX640 laser light source. *Black* camera pulses are recorded images. The *y*-axis shows normalized voltage signals used to trigger various operations in the experiment

constant 2.5 A delivered to the bridgewire by the LDD. Then, bridgewire rupture triggered the start of image collection. As will be shown later, the shock wave had already formed and expanded to a radius of the order of 2–4 cm within the surrounding environment for all experiments before bridgewire rupture and the first image was collected. The laser was pulsed for a total of 120 laser pulses at 500 kHz and 250 ns pulse width. The camera recorded image sequences with 102 frames at 500 kHz and 250 ns exposure. The laser pulses and camera images were synchronized as shown in Fig. 4.

4 Schlieren images and analysis methods

Each test captured a 102-frame image sequence of the environment surrounding the igniter. Nominally, 60 frames of the full image sequence captured the blast wave propagation within the field of view. For a representative middle density TKP test (T2), the images are presented in terms of a composite image to show shock wave shape evolution (Fig. 5a) and three individual frames to show the multiphase output (Fig. 5b–d). Corresponding images for a representative middle density THKP test (TH2) appear in Fig. 6. All schlieren images given here and in the following sections (with the exception of Fig. 7) have had a gamma correction applied only to improve contrast to aid the reader.

The open top of the charge cavity containing the pyrotechnic pressed powder is located near the bottom right corner of the images. In all image sequences, the nearly hemispherical primary shock wave extends across the image field of view and propagates radially away from the igniter position (Figs. 5a, 6a). Evidence of a Mach reflection, from the solid boundary of the igniter body and v-block mounting hardware, is evident from the triple point at the intersection of the incident wave, reflected wave, and Mach stem. Behind the shock is an optically dense volume of gaseous combustion prod-

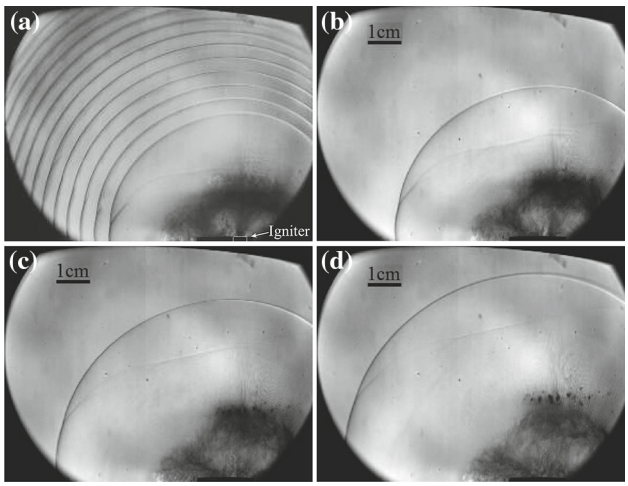

Fig. 5 Frames are shown from a representative TKP igniter (T2). The first composite frame shows the shock wave shape evolution in time, shown every fifth frame until no longer visible in the field of view. The subsequent frames are 20 μs apart, showing the gas volume expansion and solid particle motion. **a** t = 0–60 μs, **b** t = 20 μs, **c** t = 40 μs, **d** t = 60 μs

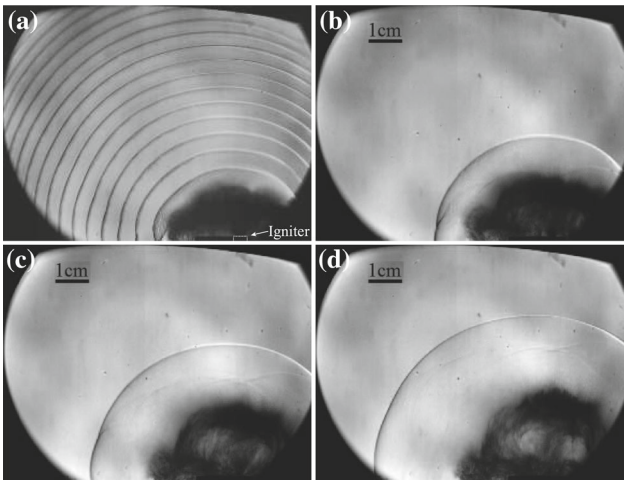

Fig. 6 Frames are shown from a representative THKP igniter (TH2). The first composite frame shows the shock wave shape evolution over time, shown every fifth frame until no longer visible in the field of view. The subsequent frames are 20 μs apart, showing the gas volume expansion and particle cloud. **a** t = 0–75 μs, **b** t = 20 μs, **c** t = 40 μs, **d** t = 60 μs

ucts and solid particles that exhibits a vertical directionality consistent with the cylindrical charge cavity axis.

In Fig. 5c, d, discrete particles or clumps of particles are observed to jet ahead of the larger opaque combustion products being ejected from the igniter. In general, solid particles were clearly observed in all of the TKP tests at the different densities. For most of the THKP tests, evidence of these discrete particles was not obvious (as in the dense cloud of Fig. 6d). For the nominal image resolution of 0.03 cm/pixel (8 cm/260 pixels along width of image), particles smaller than 0.6 mm in size (2 pixels) cannot be resolved at this image magnification. Considering the initial particle sizes of the pyrotechnic constituents (ranging from 13–22 μm), it is reasonable to assume that if discrete particles are visible in the images, then these must consist of clumps of the initial pressed powder bed that have been expelled from the charge cavity due to the growth of a pressure gradient within the bed or perhaps from the occurrence of transition to the deconsolidated burning regime within the charge cavity. An area of future work would be to increase the magnification or to couple in-line digital holography [26] for improved measurement of the particulate size distribution.

4.1 Shock wave equations

Time histories of the shock front radius were extracted from the image sequences and a least squares fit to the functional form of the blast wave equation [27,36] was performed. The shock speed and Mach number were found by pointwise differentiation of the shock motion. The ambient air conditions were assumed to be constant with a sound speed

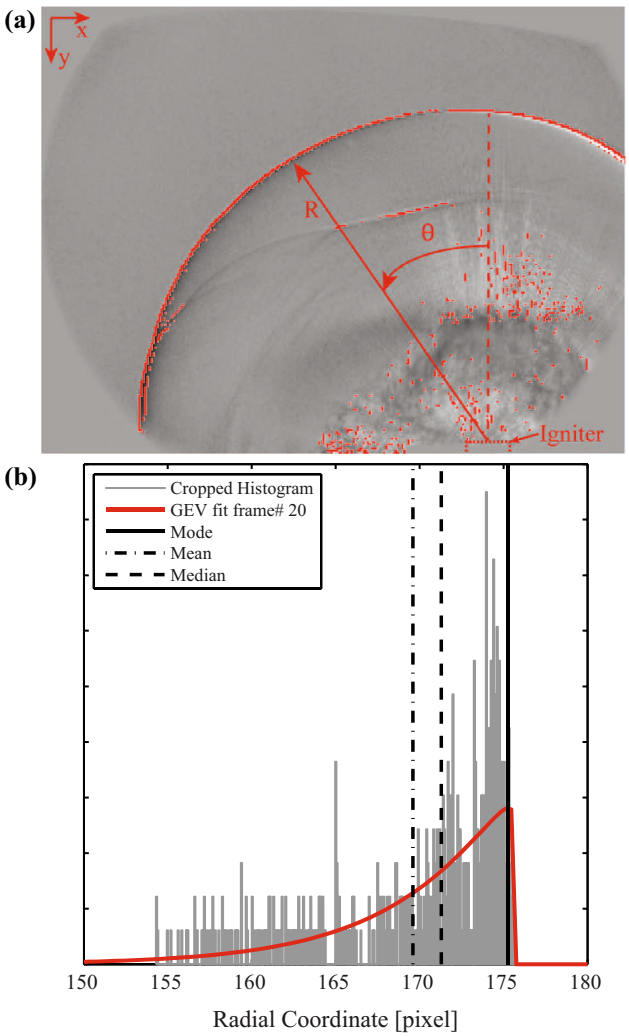

Fig. 7 **a** Image-processing methodology showing radius extraction coordinates on a representative frame from the T2 image sequence (Fig. 5c). **b** Histogram of radial coordinates from the above frame showing the probability density function of the generalized extreme value distribution fit to data and three statistical characteristics of this distribution

a_0 = 340 m/s and γ = 1.4. An ambient pressure of P_0 = 83.7 kPa was assumed based on typical conditions in Albuquerque, NM. Finally, the one-dimensional Rankine–Hugoniot equations were used to determine the pressure rise across the shock wave [37].

4.2 Shock tracking methodology

MATLAB® [38] was used to process the recorded image sequences to detect and track the shock front position as a function of time from the stationary igniter location [35]. Figure 7a shows one frame (also shown in Fig. 5c), illustrating the shock front tracking methodology.

An image mask and average background image were subtracted from each raw image to enhance the shock wave

feature. The shock front edge (and other undesired edges around the solid particles) was detected with *edge* function from the Image Processing Toolbox in MATLAB ® (Fig. 7a) [35]. A polar coordinate transformation (Fig. 7a) was applied to the identified edge pixels of each frame, resulting in values of $[R(t), \theta(t)]$. These $[R(t), \theta(t)]$ data enabled a quantifiable assessment of the hemispherical shape of the shock wave (via the distribution of R values at a given time across all values of θ).

Previously, the shock front was tracked along rays at constant values of $\theta = 0°, 45°, 90°$ extending from the exit plane of the igniter into the surrounding environment [35]. Here, a statistical approach that represents the shock front position with a single characteristic radius is presented. This method reduces the distribution of all measured $[R(t), \theta(t)]$ values to a single characteristic shock radius $\bar{R}(t)$ with associated confidence level of the fitted value. The probability distributions of R at all values of θ were plotted for each frame (Fig. 7b) and modeled with the generalized extreme value (GEV) statistical distribution [39]. The fitted GEV distribution appears in Fig. 7b as a solid curve. The mode of the GEV probability distribution function (solid vertical line of Fig. 7b) was selected to represent a single characteristic shock radius $\bar{R}$ at time t.

To assess the factors affecting the shock wave symmetry, the variation of R as a function of θ was studied. The observed Mach reflection accelerates the wave slightly at values of $\theta \to 90°$, as does the directionality of the cylindrical charge cavity at values of $\theta \approx 0°$. For the data of Fig. 7b, the variation in radius is nominally 20 pixels. This can be considered in the context of the arc length of the visible portion of the shock wave (≈400 pixels). Thus, the variation in radius was approximately 5 % of the visible shock front length. Similar quantification at all other times found this variation to remain nominally constant.

4.3 Uncertainty quantification

The temporal uncertainty is dependent on the camera exposure time. The spatial uncertainty is dependent on image warping due to the curved lenses, the demagnified field of view, and the process used to locate the edge of the shock wave. Image scaling was performed by imaging a 3.2 mm × 3.2 mm grid using the schlieren diagnostic and calculating average scale parameters along the horizontal and vertical directions of the image matrix. Thus, the pixel distances were converted to physical distances and the corresponding shock front radius, as shown in (1):

$$(R \pm \varepsilon_R)^2 = [(\Delta X \pm \varepsilon_{S.L.})(S_{row} \pm \sigma_{row})]^2 + [(\Delta Y \pm \varepsilon_{S.L.})(S_{colm} \pm \sigma_{colm})]^2, \quad (1)$$

Table 2 Uncertainty values for schlieren data

Parameter	Value
ε_t	±125 ns
$\varepsilon_{S.L.}$	±1 pixel
S_{row}	0.0297 cm/pixel
σ_{row}	±0.0015 cm/pixel
S_{colm}	0.0300 cm/pixel
σ_{colm}	±0.0020 cm/pixel

where ε_R is the uncertainty in the radius, ΔX the difference in row values between the center of the reaction and the shock location, $\varepsilon_{S.L.}$ the uncertainty in shock location found by the schlieren image analysis code estimated at ±1 pixel accuracy, S_{row} the average scale factor in the x-direction, σ_{row} the standard deviation of the scale factor in the x-direction, ΔY the difference in column values between the center of the reaction and the shock location, S_{colm} the average scale factor in the y-direction, and σ_{colm} the standard deviation of the scale factor in the y-direction. The uncertainty of the radius was found through the propagation of error for (1). Table 2 summarizes values used to calculate the uncertainties in the data extracted from the schlieren image sequences.

The uncertainty of $\bar{R}(t)$ consists of contributions from the uncertainty in R and the uncertainty in the GEV model. The uncertainty in R is calculated with (1). The uncertainty of the GEV model is considered to be the difference between the 95 % confidence interval bounds and the value of $\bar{R}$. For example, for the shock front of Fig. 7, $\bar{R} = 5.23 \pm 0.21$ cm. Here, the uncertainty in $\bar{R}$ comprises the uncertainty in the radius values due to the image uncertainty (±0.18 cm) plus the uncertainty associated with the statistical distribution about the characteristic radius (±0.03 cm).

Shock speed is found by pointwise differentiation of the $\bar{R}(t)$ data (2).

$$U \pm \varepsilon_U = \frac{\Delta \bar{R} \pm \varepsilon_{\Delta \bar{R}}}{\Delta t \pm \varepsilon_{\Delta t}}. \quad (2)$$

For example, the shock front of Fig. 7 has a calculated Mach number of 1.04 ± 0.28. This can be compared to the simplest representation of the experimental velocity resolution considering the image resolution ≈0.03 cm/pixel × 0.03 cm/pixel and the 2 μs interframe time. Here, the sensitivity of the shock velocity measurement is between 0.15 mm/μs and 0.21 mm/μs depending on whether a vector velocity at the shock front is aligned with the pixel edges (as is the case when $\theta = 0°$ or 90°) or diagonally crossing the pixel at $\theta = 45°$.

5 Igniter output

For each test condition of Table 1, the $\bar{R}(t)$ data were extracted. Figure 8 plots the results of the representative TKP igniter of Fig. 5 and the representative THKP igniter of Fig. 6. $t = 0$ corresponds to the camera trigger time after bridgewire rupture. Both datasets were fitted to the blast wave equation (Sect. 4.1). The fitted equations are plotted within the extent of the experimental data in Fig. 8 as solid lines.

The corresponding Mach numbers are plotted with respect to $\bar{R}(t)$ in Fig. 9 for the same TKP and THKP igniters of Fig. 8. The derivative of the fitted blast wave equation is plotted within the extent of the experimental data as a solid line. The pointwise differentiation of the $\bar{R}(t)$ data to determine the corresponding shock speed increases the observed scatter. Another contribution to the scatter is related to the statistical representation of the entire visible shock front, which

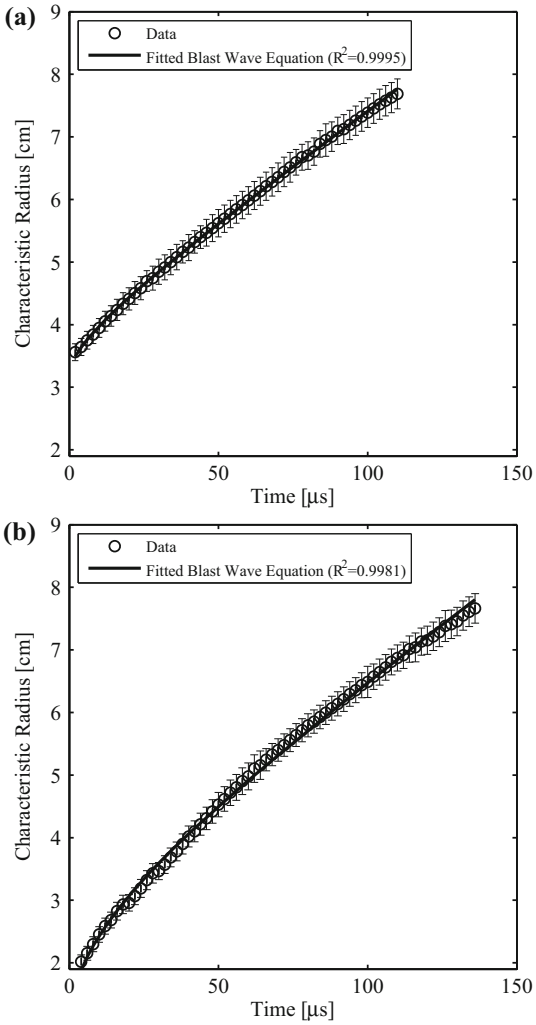

Fig. 8 Plot of characteristic radius versus time for **a** TKP igniter (T2 of Fig. 5) and **b** THKP igniter (TH2 of Fig. 6). $t = 0$ corresponds to the camera trigger time after bridgewire rupture

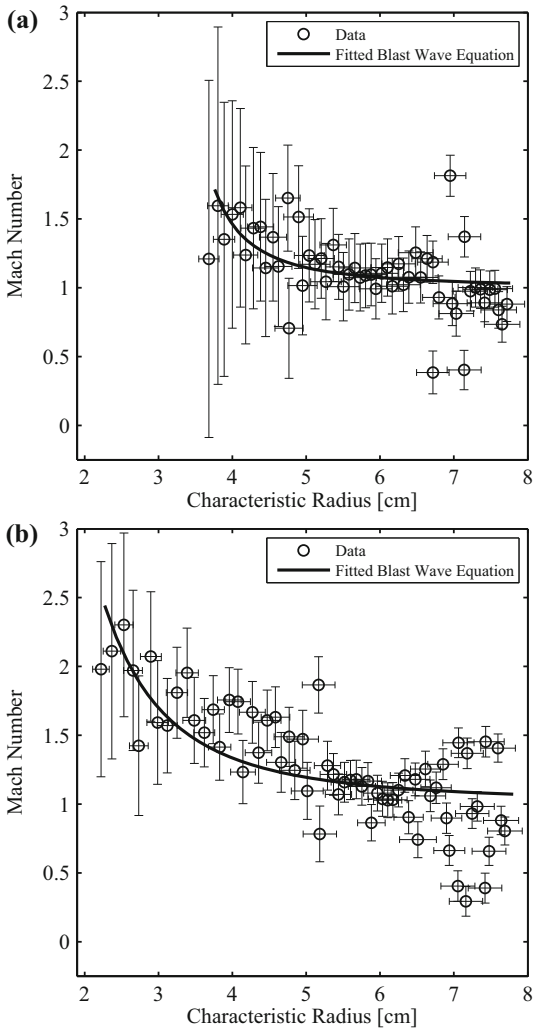

Fig. 9 Plot of Mach number versus characteristic radius for **a** TKP igniter (T2 of Fig. 5) and **b** THKP igniter (TH2 of Fig. 6)

becomes smaller in time as the shock front exits different regions of the image at different radii. One of the first portions of the shock wave to exit the field of view is the data at $\theta \rightarrow 90°$. Next, the shock wave exits the field of view out the top of the image. Afterward, only a narrow portion of the shock front remains visible ($40° < \theta < 60°$) and gets decreasingly shorter in time. Each time a portion of the shock front exits the field of view, the statistical distribution is fitted to a smaller sample of the entire shock front. The effect of this is most evident in the increased scatter of both the characteristic radius and Mach number at radius values larger than about 6–6.5 cm. Clearly, increasing the image resolution (through a larger camera CCD), a slower recording rate, or larger optics to prevent cropping the visible regions of the shock front would contribute to decreasing this observed scatter. However, for the large field of view and fast frame rate used in these tests, the shock decay toward near-sonic conditions is evident.

Repeat tests were performed for most of the test parameters of Table 1. A single test was conducted for conditions T1 and T3, two repeat tests were conducted at condition TH3, and three repeat tests were conducted at conditions T2 and TH2. Since the blast wave equation is shown to correlate with the data within the experimental uncertainties and provides a simplified view of the shock behavior (Fig. 9), the fitted curve for each test is used to compare results between the research igniter parameters of material and density in Fig. 10. The comparisons are thus not complicated by the data scatter of the pointwise differentiation of the radius data. Each curve is plotted only within the extent of the experimental data.

For a pyrotechnic igniter, it is expected that the shock Mach number, as plotted in Fig. 10, should decay to Mach 1 (sound wave) within a short distance. In all cases, the measured shock velocities are between Mach 1 and Mach 2.5 and decay to near-sonic conditions within the experimental field of view as expected.

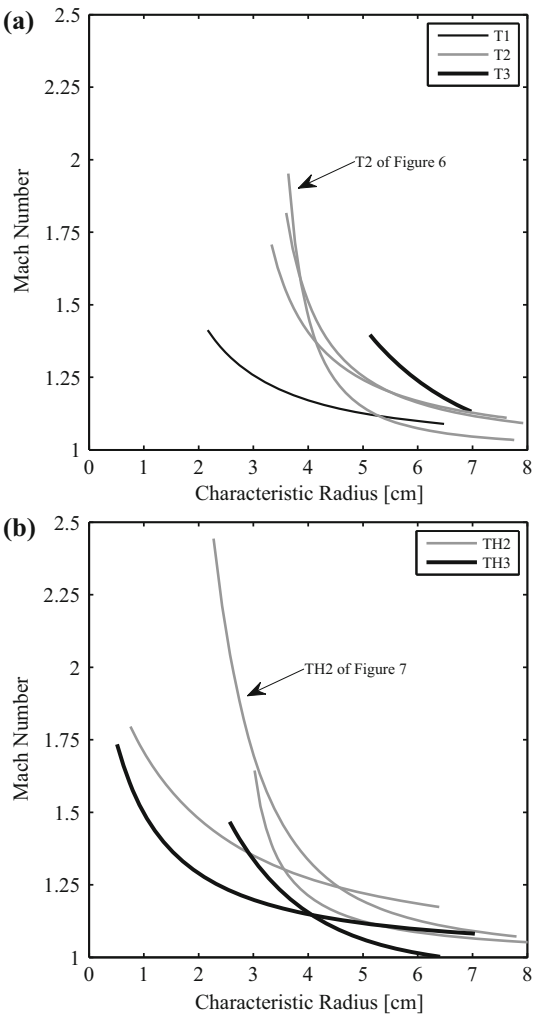

Fig. 10 Comparison of the fitted blast wave equation curves plotted in terms of Mach number versus characteristic radius for the **a** TKP tests and **b** THKP tests of Table 1. The *thick black lines* represent the highest density tests (T3 and TH3), the *thick gray lines* represent the middle density tests (T2 and TH2), and the single low density test is shown as a *thin black line* (T1)

At a given radius from the igniter, it is expected that the shock strength (Mach number) should increase for an increased energy content of the pyrotechnic: higher density charges should produce stronger shock waves, and higher energy density materials (THKP) should produce stronger shock waves than lower energy density materials (TKP). The TKP curves in Fig. 10a show the expected behavior of increased shock speed for increased charge density from T1 to T2 to T3 (see Table 1). The region of data overlap is limited due to the experimental time delay, but this delay further demonstrates that the T3 shock wave is fastest because it has propagated to the largest radius before the image recording begins. In contrast, for the slowest shock (T1) the image collection begins when the shock has only expanded to approximately 2 cm.

The repeatability of the three T2 tests is demonstrated and is quite good considering our research igniters contained inherent stochastic variability associated with the bridgewire–powder interface due to the following factors: (1) no axial confinement at the exit plane of the charge cavity to ensure consistent thermal contact resistance between the bridgewire and neighboring pyrotechnic material; and (2) differences in the powder contact area and mesostructure of the pyrotechnic powder volume in the vicinity of the bridgewire from the single increment powder pressing operation.

The THKP curves of Fig. 10b exhibit an unexpected decrease in shock strength with increasing pyrotechnic density: the high-density TH3 tests generate weaker shock waves than the lower-density TH2 tests. This is not only noted in terms of the shock speed at a given radius, but also in the radius at the start of image collection. These THKP tests have repeatability that is notably worse that the TKP (T2) tests. It is difficult to discern the reason for these differences with only the quantitative data of shock motion, but an analysis of the corresponding full-field images for qualitative assessment of the multiphase flow provides some insights.

Shown in Fig. 11 are two frames from one of the TH3 tests, zoomed in to a smaller region around the igniter. The

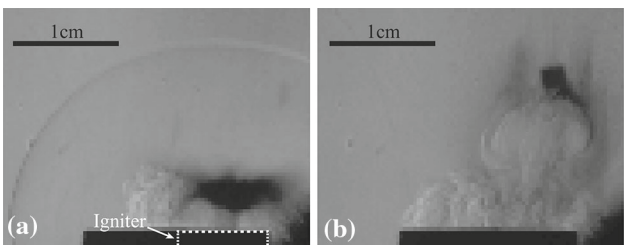

Fig. 11 Two frames zoomed in near the igniter are shown from an "incomplete" THKP test (TH3). The frames are 160 μs apart. **a** t = 20 μs, **b** t = 180 μs

left image shows a weak shock as noted by little image contrast, indicative of a minimal schlieren effect at the front. The visible combustion products cover a much smaller region of the image relative to the igniter compared with the images at the same 20 μs time in Figs. 5b and 6b. In the right image of Fig. 11, this small release of combustion products has caused a seemingly intact slug of pressed pyrotechnic material to be expelled from the charge cavity and, in fact, a slug of material was found intact inside the combustion chamber after the test. The physical dimensions of this slug correspond closely to the diameter of the charge cavity, indicating that this is unconsumed material from within the charge cavity. If a significant fraction of the TH3 pyrotechnic powder did not burn within or external to the charge cavity, then shock strength is expected to be notably lower, as quantitatively shown in Fig. 10b. We refer to the tests showing features qualitatively similar to this example as having "incomplete" combustion, and all TH3 tests exhibited this behavior. This suggests that a region of the pyrotechnic bed near the bridgewire ignited and began to conductively burn, but was subsequently quenched. The images captured here are the first to show this process with such image clarity.

Visualization of these cases where the pyrotechnic material is largely unreacted provides new and unique insights into the role of the EED design (e.g., the importance of the interface between the powder and bridgewire) and the need for better understanding of pyrotechnic combustion behavior within these geometries (e.g, transition from steady to deconsolidate burn or even a quenching of the burn front). When this visualization capability is coupled with the demonstrated statistical analysis of the shock motion, the potential for advancing the design, testing, and validation approaches within the field of EED design is quite exciting.

6 Scaling considerations

To compare the data across all experimental parameters, a pressure ratio $\Delta P/P_0$ and non-dimensional distance $Z = \bar{R}(t)/L_e$ from the igniter are used as scaled parameters. The pressure ratio is calculated from the measured shock Mach number scaled to atmospheric pressure P_0. The shock wave radius is scaled with the explosion length $L_e = (E/P_0)^{1/3}$, which assumes spherical symmetry and includes an energy term, allowing for scaling between materials with different energy contents [33]. For these pyrotechnic mixtures in the small EED geometries, the simplest choice for the explosion length scaling, E, is the constant volume explosion energies of Table 1. The data from Fig. 10 are scaled using this approach, and the results are plotted in Fig. 12.

The data in Fig. 12 allow comparisons between the two pyrotechnic materials. These data are effectively a per-unit-mass-basis comparison between the different materials via

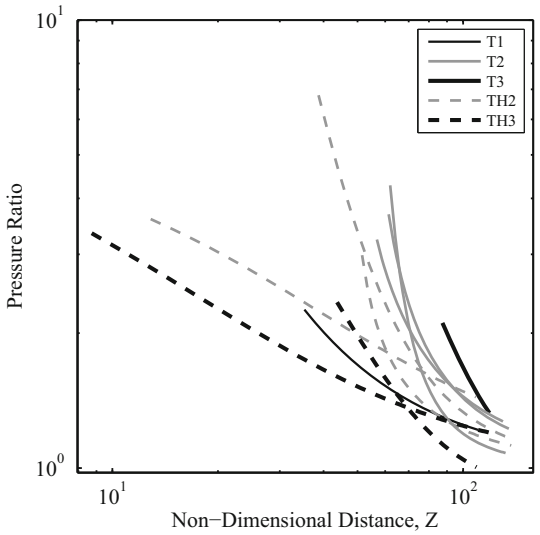

Fig. 12 Scaled comparison of TKP and THKP performance in terms of non-dimensional pressure versus non-dimensional distance from the igniter exit plane

the non-dimensionalization with the total energy E. The data show that the TH2 charges produce a similar output as the T2 charges, although not as repeatable. The T3 pyrotechnics produce the largest scaled output. The "incomplete" combustion TH3 tests have wide variability, further indicating that the material did not burn completely and that only a small fraction of the total available chemical energy was released to support the shock.

Variations in the pyrotechnic EED design that affect the time or length scales of energy deposition and the multiphase combustion product composition will certainly affect the resulting mechanical energy associated with the shock front. Thus, comparisons of shock wave data, plotted in terms of scaled parameters, from the output of EEDs with varying pyrotechnic constituents, device confinement, or conditions at the hotwire–powder interface could be used for assessing design decisions.

7 Conclusion

A high-speed schlieren imaging diagnostic system for observing subsonic and supersonic multiphase material motion from the initiation of two types of titanium-based pyrotechnic igniters into the surrounding environment has been designed and built. The diagnostic system recorded temporally and spatially resolved data that was applied to the quantitative characterization of the output from TKP and THKP igniters. This diagnostic system succeeded through its ability to overcome the intense self-illumination from the pyrotechnic combustion using non-coherent laser source illumination from the SILUX640 laser system. The use of

non-coherent laser light preserved the excellent resolution of weaker gas dynamic features that were visualized using schlieren techniques.

The resulting image sequences showed shock motion that was different between TKP and THKP igniters for the bulk powder densities tested. Images of the shock wave propagation were reduced to a single characteristic radius as a function of time that was further analyzed in terms of the shock velocity, Mach number, and pressure ratio. We have demonstrated this experimental analysis and methodology for comparison of EED designs aimed at maximizing the mechanical energy associated with the shock front. The demonstrated approach is recommended for future EED evaluation, because the shock wave motion is strongly dependent on factors affecting the time and length scale of the energy deposition, which are not easily measured through other approaches.

Acknowledgments The authors are especially grateful to Ian Kohl and Michael Oliver for their guidance and assistance in conducting these experiments. The significant contributions of Alex Tappan, Jill Miller, Duane Richardson, Cody Love, Adam Sapp, Ryan Marinis, and Wayne Trott to different aspects of the experiments are also gratefully acknowledged. The authors appreciate the many helpful discussions with Bill Erikson. Sandia National Laboratories is a multi-program laboratory managed and operated by Sandia Corporation, a wholly owned subsidiary of Lockheed Martin Corporation, for the U.S. Department of Energy's National Nuclear Security Administration under contract DE-AC04-94AL85000. Unlimited release, SAND2014-4641J.

References

1. Rosenthal, L.: Electro-thermal equations for electro-explosive devices. Technical Report. NavOrd 6684, U.S. Naval Ordinance Laboratory (1959)
2. Bickes Jr., R., Schlobohn, S., Ewick, D.: Semiconductor bridge (SCB) igniter studies: I. Comparison of SCB and hot-wire pyrotechnic actuators. In: Proceedings of the 13th International Pyrotechnics Seminar, pp. 69–80. International Pyrotechnics Society, Grand Junction, July 11–15 (1988)
3. Wilcox, P.: Pyrotechnic device technology. Technical Report. SAND90-0259C, Sandia National Laboratories (1990)
4. Begeal, D., Stanton, P.: Pyrotechnic deflagration velocity and permeability. In: Proceedings of the 8th International Pyrotechnics Seminar, pp. 112–128. International Pyrotechnics Society, Steamboat Springs, July 12–16 (1982)
5. Fathollahi, M., Pourmortazavi, S., Hosseini, S.: The effect of the particle size of potassium chlorate in pyrotechnic compositions. Combust Flame **138**, 304–306 (2004)
6. Berger, B.: Parameters influencing the pyrotechnic reaction. Propellants Explos Pyrotech **30**, 27–35 (2005)
7. Cooper, M., Oliver, M.: The burning regimes and conductive burn rates of titanium subhydride potassium perchlorate ($TiH_{1.65}/KClO_4$) in hybrid closed bomb-strand burner experiments. Combust Flame **160**, 2619–2630 (2013)
8. Weismiller, M., Malchi, J., Lee, J., Yetter, R., Foley, T.: Effects of fuel and oxidizer particle dimensions on the propagation of aluminum containing thermites. Proc. Combust. Inst. **33**(2), 1989–1996 (2011)
9. Moore, K., Pantoya, M., Son, S.: Combustion behavior resulting from bimodal aluminum size distributions in thermites. J. Propuls. Power **23**(1), 181–185 (2007)
10. Aly, Y., Schoenitz, M., Dreizin, E.: Ignition and combustion of mechanically alloyed Al_2Mg powders with customized particle sizes. Combust Flame **160**, 835–842 (2013)
11. Edington, J., Baumann, J.: Thermal battery igniter activation measurements and flow modeling. In: Proceedings of the 45th Power Sources Conference, pp. 457–460. Power Sources Conference, New York, NY. Las Vegas, NV, USA, June 11–14 (2012)
12. Buttigieg, G., Paine, G., Hsiao, R.: Shock tube effect inside a pyrotechnic igniter. Propellants Explos. Pyrotech. **40**(5), 743–748 (2015)
13. Jackson, S.: Deflagration phenomena in energetic materials: an overview. In: Asay, B. (ed.) Non-Shock Initiation of Explosives. Shock Wave Science and Technology Reference Library, vol. 5, chap. 5, pp. 245–292. Springer, Berlin (2010)
14. Kuo, K., Summerfield, M.: Fundamentals of solid-propellant combustion. In: Progress in Astronautics and Aeronautics, vol. 90. American Institute of Aeronautics and Astronautics, New York (1984)
15. Fifer, R., Cole, J.: Transitions from laminar burning for porous crystalline explosives. In: Short, J.M. (ed.) Proceedings of the International Symposium on Detonation (7th), pp. 164–174. Defense Technical Information Center, Annapolis, June 16–19 (1981)
16. Holy, J.: Pressure dependent burn rates of $TiH_x/KClO_4$ (x = 0.2, 0.65, 1.65). In: Proceedings of the 11th International Pyrotechnics Seminar, pp. 327–344. International Pyrotechnics Society, Vail, July 7–11 (1986)
17. Robertson, M., Igel, E.: High speed optical studies of pyrotechnic initiation phenomena. In: Proceedings of the 5th International Pyrotechnics Seminar, pp. 485–501. International Pyrotechnics Society, Vail, July 12–16 (1976)
18. Nojima, T., Hara, K., Hasegawa, T., Iwakura, M., Hosoya, F., Yoshida, T.: Burning behavior of high explosives and pyrotechnic compositions. In: Proceedings of the 20th International Pyrotechnics Seminar, pp. 769–778. International Pyrotechnics Society, Colorado Springs, July 25–29 (1994)
19. Hingorani-Norenberg, S., Razani, A., Shahinpoor, M.: Compaction of $TiH_{1.65}/KClO_4$ pyrotechnic powder during confined burn. Technical Report. SAND90-0600C, Sandia National Laboratories (1990)
20. Hingorani-Norenberg, S.: An experimental study of the burn rate of $TiH_{1.65}/KClO_4$ pyrotechnic under confinement. Technical Report. SAND88-2393, Sandia National Laboratories (1988)
21. Dosser, L., Reed, J., Stark, M.: Laser illuminated high speed photography of energetic materials and components with a copper vapor laser. In: Sze, R., Duarte, F. (eds.) Proceedings of the International Conference on Lasers '88, pp. 655–657. Society for Optical and Quantum Electronics, STS Press, Lake Tahoe, December 7–11, 1987 (1989)
22. Dosser, L., Guidotti, R.: Characterization of energetic devices for thermal battery applications by high speed photography. Technical Report. SAND93-2732C, Mound Applied Technologies (1993)
23. Evans, N.: Igniter and actuator output testing. In: Proceedings of the 13th International Pyrotechnics Seminar, pp. 243–262. International Pyrotechnics Society, Grand Junction, July 11–15 (1988)
24. Evans, N., Durand, N.: Heat transfer characteristics of igniter output plumes. In: Proceedings of the 14th International Pyrotechnics Seminar, pp. 173–184. International Pyrotechnics Society, Jersey, September 18–22 (1989)
25. Murphy, M., Adrian, R., Stewart, D., Elliott, G., Thomas, K., Kennedy, J.: Visualization of blast waves created by exploding bridge wires. J. Vis. **8**(2), 125–135 (2005)
26. Guildenbecher, D., Cooper, M., Gill, W., Stauffacher, H., Oliver, M., Grasser, T.: Quantitative, three-dimensional imaging of alu-

minum drop combustion in solid propellant plumes via digital in-line holography. Opt. Lett. **39**(17), 5126–5129 (2014)
27. Kleine, H., Dewey, J., Ohashi, K., Mizukaki, T., Takayama, K.: Studies of the TNT equivalence of silver azide charges. Shock Waves **13**(2), 123–138 (2003)
28. Kleine, H., Timofeev, E., Takayama, K.: Laboratory-scale blast wave phenomena–optical diagnostics and applications. Shock Waves **14**, 343–357 (2005)
29. Hargather, M., Settles, G.: Optical measurement and scaling of blasts from gram-range explosive charges. Shock Waves **17**, 215–223 (2007)
30. Baker, W.E.: Blast scaling. In: Explosions in Air. University of Texas Press, Austin and London (1973)
31. Wild, R.: Propagation of blast waves produced by a pyrotechnic mixture. J. Hazard. Mater. **7**, 75–79 (1982)
32. DeYong, L., Campanella, G.: A study of blast characteristics of several primary explosives and pyrotechnic compositions. J. Hazard. Mater. **21**, 125–133 (1989)
33. Baker, W., Cox, P., Westine, P., Kulesz, J., Strehlow, R.: Free-field explosions and their characteristics. In: Explosion Hazards and Evaluation. Fundamental Studies in Engineering, vol. 5, chap. 2, pp. 106–122. Elsevier Scientific Publishing Company, New York (1983)
34. Bastea, S., Fried, L.: Cheetah 7.0 user's manual. Technical Report. LLNL-SM-599073, Lawrence Livermore National Laboratory (2012)
35. Skaggs, M.: Characterization of pyrotechnic igniter output with high-speed schlieren imaging. Master's thesis, New Mexico Institute of Mining and Technology (2014)
36. Dewey, J.: Explosive flows: shock tubes and blast waves. In: Yang, W. (ed.) Handbook of Flow Visualization, chap. 29. Hemisphere, New York (1989)
37. Thompson, P.: Compressible Fluid Dynamics. McGraw-Hill Inc., London (1988)
38. MATLAB: version 8.3.0.532 (R2014a). The MathWorks Inc., Natick, Massachusetts (2014)
39. Coles, S.: An Introduction to Statistical Modeling of Extreme Values. In: Springer Series in Statistics, vol. 208. Springer, London (2001)